



Wave packet scattering from time-varying potential barriers in one dimension

Robert M. Dimeo

Citation: [American Journal of Physics](#) **82**, 142 (2014); doi: 10.1119/1.4833557

View online: <http://dx.doi.org/10.1119/1.4833557>

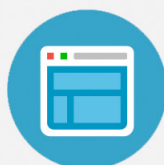
View Table of Contents: <http://scitation.aip.org/content/aapt/journal/ajp/82/2?ver=pdfcov>

Published by the [American Association of Physics Teachers](#)



Re-register for Table of Content Alerts

Create a profile.



Sign up today!



COMPUTATIONAL PHYSICS

The Computational Physics Section publishes articles that help students and their instructors learn about the physics and the computational tools used in contemporary research. Most articles will be solicited, but interested authors should email a proposal to the editors of the Section, Jan Tobochnik (jant@kzoo.edu) or Harvey Gould (hgould@clarku.edu). Summarize the physics and the algorithm you wish to include in your submission and how the material would be accessible to advanced undergraduates or beginning graduate students.

Wave packet scattering from time-varying potential barriers in one dimension

Robert M. Dimeo^{a)}

National Institute of Standards and Technology, 100 Bureau Drive, MS 6100, Gaithersburg, Maryland 20899

(Received 24 October 2013; accepted 12 November 2013)

We discuss a solution of the time-dependent Schrödinger equation that incorporates absorbing boundary conditions and a method for extracting the reflection and transmission probabilities for wave packets interacting with time-dependent potential barriers. We apply the method to a rectangular barrier that moves with constant velocity, an oscillating rectangular barrier, a locally periodic barrier with an amplitude modulated by a traveling wave, and a locally periodic potential with an amplitude modulated by a standing wave. Visualizations of the reflection phenomena are presented with an emphasis on understanding these systems from their dynamics. Applications to non-stationary neutron optics experiments are discussed briefly. © 2014 American Association of Physics Teachers.

[<http://dx.doi.org/10.1119/1.4833557>]

I. INTRODUCTION

The reflection and transmission of matter waves from static potential barriers have been studied extensively using theoretical, numerical, and experimental techniques. Moreover, computer visualizations of wave packet scattering from barriers and wells have been used to gain insight into transmission and reflection phenomena ever since the paper by Goldberg, Schey, and Schwartz.¹ Nevertheless, visualizing wave packet scattering from time-varying potential barriers has not featured as prominently in the literature. Yet a numerical approach in which the time-dependent Schrödinger equation (TDSE) is solved for wave packets incident on time-varying potential barriers can offer just as powerful a tool in gaining understanding of scattering in non-stationary systems where analytical solutions are either extremely difficult or impossible to obtain. In 1982, Haavig and Reifenberger investigated the effects of modulating the height of a rectangular barrier on the transmission and reflection of a wave packet.² They used a variant of the algorithm used in Ref. 1 to solve the TDSE numerically and generated animated sequences of the time-development of the scattered wave packets. They observed that reflected wave packets showed multiple peaks that moved at different velocities, a result that they described in terms of multi-phonon exchange. One of their goals was to use their results to help design experiments to measure the effects of the dynamic image potential for charged particles. More recently numerical approaches have been used to examine the effect of barrier oscillation on resonant tunneling and particle capture by a moving potential.^{3,4}

There are many practical problems that involve solutions to the one-dimensional Schrödinger equation. For example, such solutions are applicable to neutron reflectometry

measurements.^{5–7} The specular reflection of neutrons from a material composed of multiple layers provides detailed information on the structure and composition of the depth profile of that material at the atomic scale. Because the direction of the momentum transfer in this geometry is normal to the material's surface, solutions to the one-dimensional Schrödinger equation are frequently used to describe many neutron reflectometry experiments.

Numerous non-stationary phenomena due to one-dimensional potentials have been explored using neutrons^{8–10} and even atoms.¹¹ It is not just fundamental measurements but often the measurement technique itself that depends on non-stationary phenomena. The operation of a high resolution neutron backscattering spectrometer depends on harmonically oscillating crystals that reflect neutrons of different energies based on the Doppler effect for matter waves. Given the ubiquity of non-stationary quantum phenomena and the relative scarcity of examples appropriate for the classroom, this paper outlines an approach that combines several computational methods that make possible straightforward and fast visualization of time-dependent wave packet scattering from time-varying potentials.

In Sec. II, we review the well-known result of scattering from a rectangular potential, specifically for plane waves and Gaussian wave packets. This result introduces the methodology we will use to calculate the reflectivity of potential barriers throughout this paper. The method is then applied to wave packets scattering from a rectangular barrier moving with constant velocity. The reflectivity is compared to the expected reflectivity based on Galilean invariance. The dynamics are next calculated for an oscillating rectangular barrier. The corresponding reflectivity is compared to that of the static rectangular barrier and the differences are discussed in terms of inelastic scattering. In Sec. III, we

examine scattering from a potential barrier whose amplitude supports a traveling wave as well as a standing wave. The reflectivity for both cases can be understood in terms of the same simple model and is discussed in terms of both a neutron scattering measurement from surface acoustic waves as well as a neutron Doppler monochromator used in a class of high-resolution neutron scattering instruments. We summarize our approach and results in Sec. IV.

II. REFLECTION FROM A RECTANGULAR BARRIER

A. Static barrier

The reflection of a plane wave from a rectangular barrier of width w , height V_0 , and location x_V has been treated in many textbooks on quantum mechanics,^{12,13} and thus we simply present the result. The potential centered at x_V is given by $V(x - x_V)$, where

$$V(\xi) = \begin{cases} V_0 & -w/2 \leq \xi < w/2 \\ 0 & \text{otherwise.} \end{cases} \quad (1)$$

For a plane wave with wave vector k_0 incident on this barrier the reflectivity is given by¹⁴

$$R(k_0) = 1 - \left[1 + \frac{1}{4} \left(\frac{k'}{k_0} - \frac{k_0}{k'} \right)^2 \sin^2(k'w) \right]^{-1}, \quad (2)$$

where $k' = \sqrt{k_0^2 - 2V_0}$. We use units such that $\hbar = m = 1$ in Eq. (2) and in the remainder of the paper.

Extending the treatment to find the reflectivity from a wave packet rather than a plane wave is straightforward.¹⁵ The wave packet is a Gaussian with the usual functional form

$$\psi(x, t = 0; x_0) = (\pi\sigma_x^2)^{-1/4} e^{-(x-x_0)^2/2\sigma_x^2} e^{ik_0(x-x_0)}. \quad (3)$$

In Eq. (3), k_0 is the central wavenumber of the momentum distribution $P(k; k_0) = |\phi(k, t = 0; k_0)|^2$, where

$$\phi(k, t = 0; k_0) = \left(\frac{\sigma_x^2}{\pi} \right)^{1/4} e^{-\frac{1}{2\sigma_x^2}(k-k_0)^2}. \quad (4)$$

The reflection of a Gaussian wave packet is thus found from

$$R(k_0) = \int dk R(k) P(k; k_0), \quad (5)$$

where $R(k)$ is given by Eq. (2).

For time-varying potentials it is not usually possible to use Eq. (5) to evaluate the reflectivity.¹⁶ Our approach is to perform a set of numerical computations in which a series of wave packets of different central wavenumber k_0 , and constant width σ_x are launched at the time-dependent potential and determine the amount reflected. Before doing this calculation with time-dependent potentials, we validate this approach for the simple case in which the barrier does not move and where we can use Eq. (5) to compare to the numerical experiments.

Numerical solutions of the dimensionless TDSE were performed using a variation of Visscher's staggered step algorithm,¹⁷ which has also been shown to be stable for time-dependent potentials.¹⁸ We tested the accuracy of the

algorithm for time-varying potentials by testing the time-invariance property of the wave function.¹⁹ Although we solve the dimensionless TDSE, interested readers can consult Appendix A for details on scaling the results to physical units. The advantages of the Visscher algorithm are that it is explicit, fast, accurate (unitary), and stable, all desirable traits when determining the reflectivity. Unfortunately, the algorithm suffers from one weakness: the wave function at the domain boundaries is zero. Thus waves that reach the boundaries are reflected. We could still perform these calculations effectively with these boundary conditions by placing the potential in the center of a very large integration domain. However, this procedure would result in very long integration times. Instead of a large integration domain we chose absorbing boundary conditions and a small integration domain.

The geometry of these computations is illustrated in Fig. 1. To determine the reflectivity accurately, it is important that the wave packets are not reflected at the boundaries. If boundary-reflected waves are present, they could add to the wave reflected from the barrier, thus erroneously increasing the reflectivity. To mitigate this effect, the Visscher algorithm was augmented to include absorbing boundary conditions, ensuring that transmitted waves that reach the right boundary are not reflected.²⁰ The absorbing boundary conditions have been combined with other methods of solving the TDSE and applied to other problems of interest.^{21,22} This implementation of Visscher's algorithm with absorbing boundary conditions is summarized in Appendix B. Interested readers are referred to Visscher and Shibata's papers for details on its development as well as the stability of this numerical approach. Suggested problems are proposed in Sec. V to guide readers through some of the steps in the algorithms.

The reflectivity and transmission probabilities are determined by recording the reflected and transmitted probability current at $x = x_r$ and $x = x_t$, respectively (see Fig. 1). The transmission probability is calculated by integrating the probability current $j(x, t)$ over time at a single position ($x = x_t$) just beyond the barrier. This integral must be performed over a duration spanning the entire scattering event (that is, waiting until the probability current has vanished at x_t). A derivation of this result is provided in Appendix C. The result is

$$T(k_0) = \int_{t=0}^{t_{\text{final}}} dt' j_{\text{trans}}(k_0, t'), \quad (6)$$

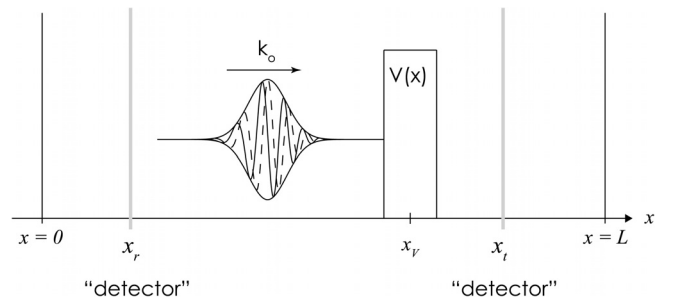


Fig. 1. Geometry used in the one-dimensional wave packet scattering events. The scattered/reflected and transmitted probability currents are recorded at x_r and x_t , respectively. The numerical integration of the TDSE is carried out over the domain $0 \leq x \leq L$ with absorbing boundaries at $x = 0$ and $x = L$.

where $j_{\text{trans}}(k_0, t) = j(x = x_t, t; k_0)$ and the probability current is given by the usual definition:

$$j(x, t) = \frac{1}{2i} \left[\psi^* \frac{\partial \psi}{\partial x} - \frac{\partial \psi^*}{\partial x} \psi \right]. \quad (7)$$

The advantage of using this method to calculate the transmission probability is that we need to sum only the probability current at a single point $x = x_t$ to find the total probability which is located in the interval $x_t \leq x < \infty$. With absorbing boundary conditions, Eq. (6) allows us to calculate the transmission probability without requiring a large domain. The other approach is to integrate the probability of the reflected wave packet. However, if the reflected wave packet has a large spatial extent and our domain is limited (that is, the reflected wave packet probability density extends over a larger range than the domain), this method will fail. Our approach allows us to simply add the contribution at a single point until such time that the current has ceased to contribute to the integral. This approach is similar to the time-of-flight technique, common to particle scattering techniques, used to record the time at which an event occurs in a detector.

To find the reflectivity $R(k_0)$ we can follow the same steps but integrate over $j_{\text{ref}}(k_0, t)$, or we can simply use Eq. (6) and calculate $R(k_0) = 1 - T(k_0)$.

To validate our approach, a series of 200 wave packets of width $\sigma_x = 0.05$ and increasing central wavenumber spanning $250 \leq k_0 \leq 850$ in equally spaced increments were scattered from a static rectangular barrier of width $w = 0.02$ and height $V_0 = 4.5 \times 10^4$. The transmitted and reflected currents were determined at $x_t = 0.23$ and $x_r = -0.025$, respectively. These points for x_t and x_r were selected to provide accurate results with a relatively small domain. A spatial grid of 2000 points was defined over $-0.3 \leq x \leq 0.25$ and a

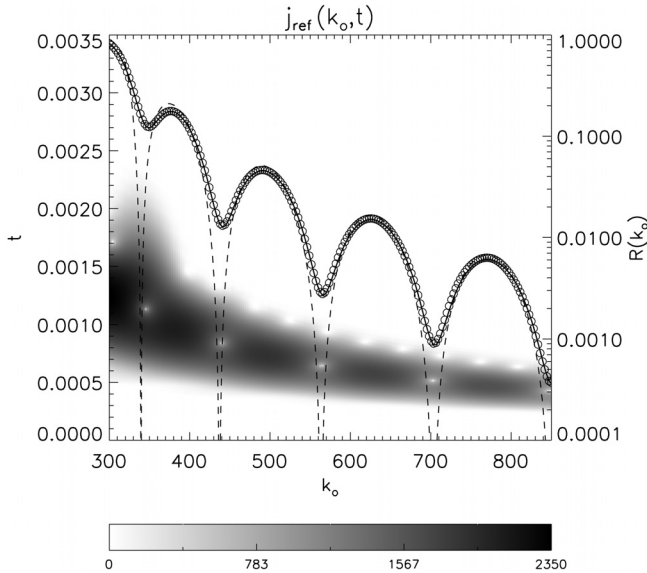


Fig. 2. Image plot of the magnitude of the probability current (log scale) and the resulting reflectivity profile for a series of 200 wave packets with width $\sigma_x = 0.05$ as a function of the central wavenumber and the time of arrival at x_r scattered from a stationary rectangular barrier of width $w = 0.02$ and height $V_0 = 4.5 \times 10^4$. The reflected current was recorded at $x_r = -0.025$. The reflection probability obtained by integrating $j_{\text{ref}}(k_0, t)$ is shown by the circle symbols. The dashed line is the reflectivity of a plane wave with wave vector k_0 from $V(x)$, given by Eq. (2). The solid line is the reflectivity calculated using Eq. (5) and the Gaussian wave packet with $\sigma_x = 0.05$.

time step of 10^{-8} was used for each update of the wavefunction. The number of time steps for each wave packet's evolution depends on the value of k_0 , but generally the wave packet evolved for 5 times the time it would take for the center of the wave packet to reach the center of the potential. Inspection of the scattering events in space-time verified that this was sufficient to capture the entire event. Furthermore, the quantity $R(k_0) + T(k_0)$, as determined by integrating $j_{\text{ref}}(k_0, t)$ and $j_{\text{trans}}(k_0, t)$, differed from unity by 10^{-7} , which is three orders of magnitude smaller than the lowest reflectivity obtained using this method.

The current at x_r , $j_{\text{ref}}(k_0, t) = j(x = x_r, t; k_0)$ is shown in Fig. 2. Note the structure in the reflected beam, notably the “holes” located at discrete points in (k_0, t) space. These are interference effects. We perform the integral

$$R(k_0) = - \int_{t=0}^{t_{\text{final}}} dt' j_{\text{ref}}(k_0, t'), \quad (8)$$

to find the reflectivity and, as shown by the circles in Fig. 2, we find excellent agreement with Eq. (5). Clearly the “holes” seen in $j_{\text{ref}}(k_0, t)$ correspond to the deep dips in $R(k_0)$.

B. Barrier moving with constant speed

A rectangular barrier moving with speed v_b can be represented by $V(x - x_V(t))$, where $V(\xi)$ is given in Eq. (1) and $x_V(t) = x_V \pm v_b t$. For a rectangular barrier that moves at constant speed, Galilean invariance requires that the reflectivity is a shifted version of the static reflectivity: $R(k_0 \pm v_b)$.¹⁰ To test this hypothesis, we recorded the reflection probability for a sequence of 200 wave packets when the barrier moved toward the wave packet with $v_b = -30$. The results of the

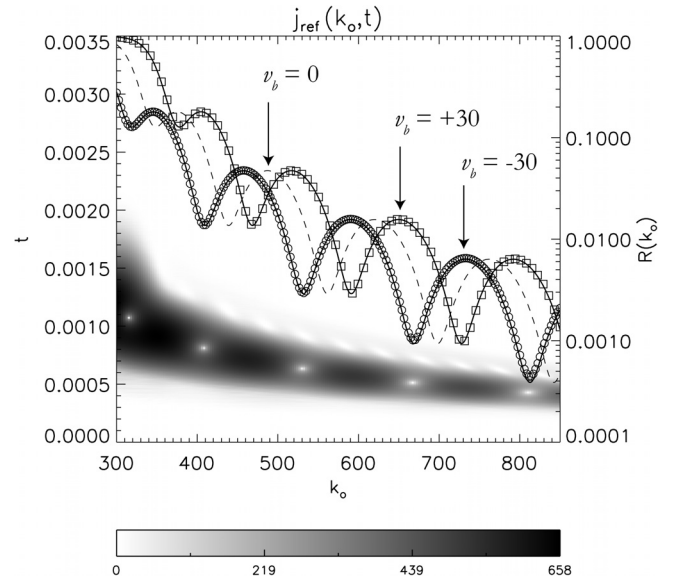


Fig. 3. Image plot of the probability current (log scale) for a wave packet with $\sigma_x = 0.05$ as a function of the central wavenumber and the time of arrival at x_r reflected from a rectangular barrier of width $w = 0.02$ and height $V_0 = 4.5 \times 10^4$ moving with a constant speed toward the wave packet ($v_b = -30$). The resulting reflectivity from the probability current is shown by the circles. The dashed line represents the reflectivity from the static barrier. The solid line through the circles is the static reflectivity shifted uniformly by $-v_b$. The square symbols denote the reflectivity from a barrier moving away from the wave packet with a constant speed. The solid line through the square symbols is the static reflectivity shifted by $+v_b$.

computations are shown in Fig. 3. It is clear that the main features of the reflected probability current observed in the static case are present in the constant-velocity case, including the well-defined holes at discrete points in (k_0, t) . The reflectivity obtained from wave packet scattering agrees with the shifted static barrier reflectivity $R(k_0 - v_b)$. The reflectivity for 80 wave packets scattered from a rectangular barrier moving away from the wave packet at constant speed ($v_b = +30$) is also shown in Fig. 3. Again, the agreement with the shifted reflectivity, $R(k_0 + v_b)$, is excellent.

C. Oscillating barrier

What is the effect on the reflected wave packet if the barrier oscillates along the x -axis? To explore this question, the methodology discussed in Sec. II A was used with the time-dependent potential $V(x - x_V(t))$, where $V(\xi)$ is given in Eq. (1) and $x_V(t) = x_V + \delta \sin \omega t$. Here, we use a value of δ that is small compared to the width w of the potential.

We use the same approach and examine the reflected and transmitted probability current for a series of 200 wave packets with wavenumbers spanning $250 \leq k_0 \leq 850$ scattered from the oscillating barrier. The barrier parameters are the same as in the static case, but the barrier oscillates with the angular frequency $\omega = 69167$ and an amplitude $\delta = 1.25 \times 10^{-3}$. The reflected probability current is shown in Fig. 4 with the resulting reflectivity plotted on top. The result for a stationary barrier is shown for comparison. The reflectivities agree only at the lowest wavenumbers ($k_0 < 330$) and start to deviate from each other significantly beyond that. The ripples seen in the static reflectivity are smoothed out, the peaks broaden, and the peaks become out of phase with those in the static case for $k \simeq 550$. Why does $R(k_0)$ for the oscillating barrier differ in this manner from that of the static barrier?

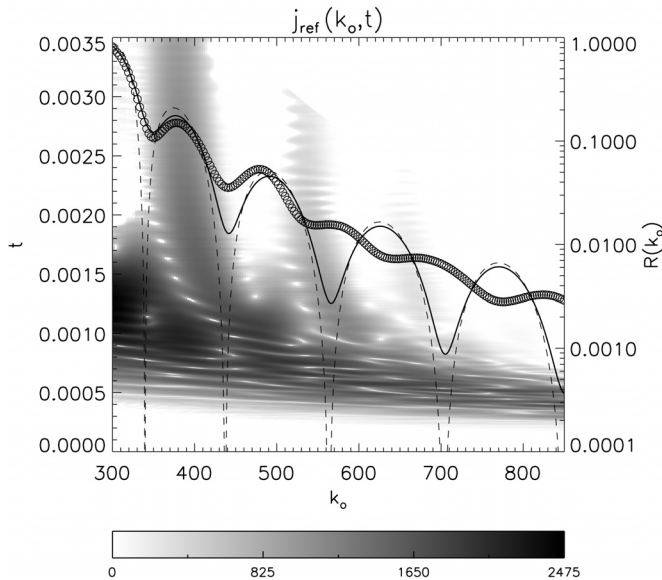


Fig. 4. Image plot of the probability current (log scale) for a wave packet with width $\sigma_x = 0.05$ as a function of k_0 and time of arrival at x_r , reflected from a rectangular barrier of width $w = 0.02$ and height $V_0 = 4.5 \times 10^4$ oscillating along the x -axis with an amplitude of $\delta = 1.25 \times 10^{-3}$ and a frequency of $\omega = 69167$. The resulting reflectivity from the probability current is shown by the circle symbols. The plane wave reflectivity and Gaussian wave packet reflectivity from a static barrier are shown in the dashed and solid lines, respectively.

The probability current for the reflected wave packet provides some clues. By comparing $j_{\text{ref}}(k_0, t)$ in Figs. 2 and 4, we see that there is additional structure for the oscillating case that is not present in the static case. One of the most prominent features in Fig. 4 is the band of reflected current that persists for long times near $k_0 = 380$. There are similar but weaker bands of current near $k_0 = 550$ and $k_0 = 650$. These reflected wave packets take longer to move past x_r and are obviously moving slower than a free wave packet of the same central incident wavenumber. Thus, these bands represent wave packet scattering events in which some significant components of the wave packet have lost energy in their interaction with the moving barrier.

The quantity $j_{\text{ref}}(k_0, t)$ shows streaks and ripples as well as the holes seen in Fig. 4. The addition of these streaks has the effect of smoothing out the deep dips in $R(k_0)$ and smoothing out the curve in general.

If we compare the evolution of the probability densities for the static and oscillating barriers, as shown in Figs. 5 and 6, respectively, we can see evidence of inelastic scattering on the final reflected wave packet. When the wave packet reflects from the stationary barrier, the final wave packet configuration has a similar, smooth Gaussian shape compared to its initial configuration. While the wave packet interacts with the barrier, much structure appears due to the interference of the reflected and incident wave components.

STATIC

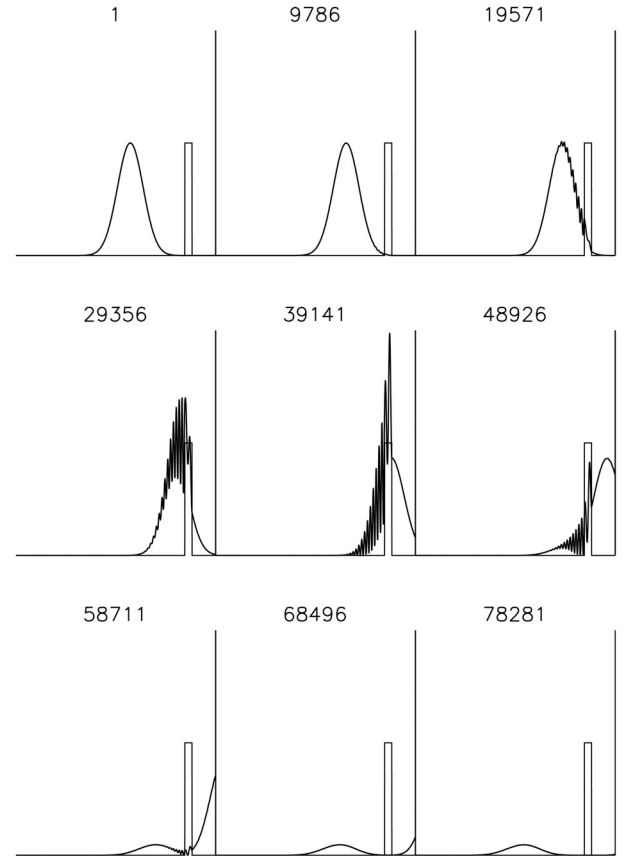


Fig. 5. Evolution of the probability density $|\psi(x, t)|^2$ for a wave packet reflecting from a static barrier; for this event, $k_0 = 400$, $V_0 = 4.5 \times 10^4$, $w = 0.02$, and $\sigma_x = 0.05$. The absorbing boundary at $x = 0.25$ is shown by the vertical line in each frame. The time step in the integration is shown at the top of each frame (enhanced online) [URL: <http://dx.doi.org/10.1119/1.4833557.1>].

OSCILLATING

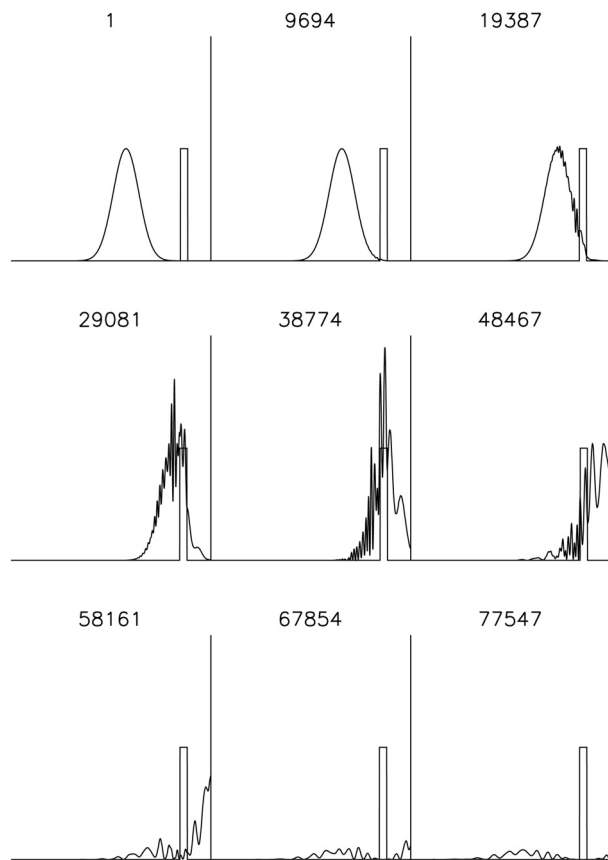


Fig. 6. Evolution of the probability density $|\psi(x,t)|^2$ for a wave packet reflecting from an oscillating barrier with $\omega = 69167$ and $\delta = 1.25 \times 10^{-3}$. All other parameters are the same as in Fig. 5 (enhanced online) [URL: <http://dx.doi.org/10.1119/1.4833557.2>].

Only after the wave packet has completely ceased interacting with the barrier does it regain its smooth, Gaussian-like shape. This well-known result has been previously observed.¹ In contrast, there is much structure in the packet reflected from the oscillating barrier after it ceases interacting with the barrier. The oscillating barrier acts like a time-varying shutter in which a series of wave packets of different speeds are reflected after interacting with the barrier. This sequence of wave packets may overlap, resulting in a wiggly envelope as can be seen in the last frame of the sequence in Fig. 6.

In addition to the visualizations in position space, which show that the wave packets have different velocity components after reflection, Fig. 7 shows that the momentum distribution of the scattered wave packet has a clear set of well-resolved peaks. In addition to the expected elastically scattered wave packet at $k_0 \simeq -400$, there are additional peaks on both sides of the elastic peak. We can explain these peaks in terms of the exchange of vibrational excitations (multi-phonon exchanges) between the wave packet and the barrier. If we treat the oscillating barrier as a quantum simple harmonic oscillator, then the final energy of the wave packet is given by

$$E_n = E_0 + n\omega, \quad (9)$$

where $E_0 = k_0^2/2$ and $n = 0, \pm 1, \pm 2, \dots$. For $n > 0$ ($n < 0$) the wave packet absorbs (emits) a phonon. We can estimate

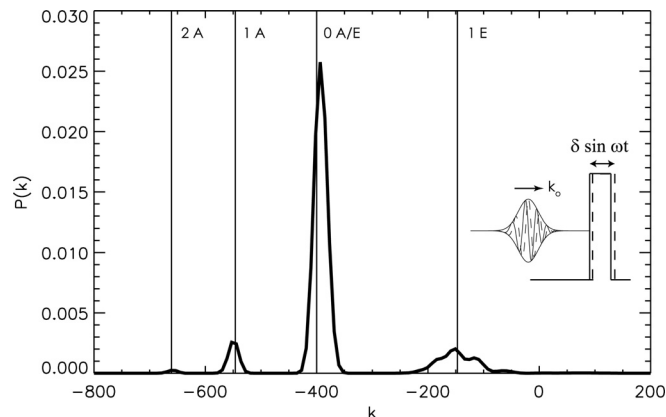


Fig. 7. The momentum distribution of a wave packet after it has reflected from an oscillating barrier; for this event, $k_0 = 400$, $V_0 = 4.5 \times 10^4$, $\delta = 1.25 \times 10^{-3}$, $w = 0.02$, $\omega = 69167$, and $\sigma_x = 0.05$. The annotations A and E preceded by a number refer to the number of phonons that the wave packet has absorbed or emitted, respectively. The vertical lines correspond to the peak locations predicted by the simple model described in the text.

the location of the peaks in the momentum distribution of the reflected wave packet using

$$k_n = -\sqrt{2E_n}, \quad (10)$$

where we have chosen the minus sign, which corresponds to a reflected wave packet.

To assess the plausibility of this simple multi-phonon model, we look at the location of the peaks in the momentum distribution in Fig. 7 and calculate the location of these peaks using Eq. (10) with $k_0 = 400$ and $\omega = 69167$. The peak associated with a zero-phonon process is the elastic peak located at $k = -400$, while the peaks associated with phonon absorption are at $k = \{-546, -661, -758\}$, as denoted by the vertical lines in Fig. 7. The peak at $k = -147$ is a one-phonon emission peak, which is allowed because the incident wave packet's energy exceeds that of one of the harmonic oscillator states of the barrier; that is, $k_0^2/2 > \omega$. Here $k_0^2/2 = 8 \times 10^4$ and $\omega = 69167$, and hence the condition is clearly satisfied. As seen in Fig. 7, the agreement between the actual peak locations and the predictions of this simple model is good. Based on the appearance of these additional discrete peaks in the momentum distribution, we conclude that there are inelastic processes involved in the interaction of the barrier and the wave packet, thus contributing to the modification of the reflectivity curve shown in Fig. 4.

The conclusion that phonons are exchanged with the potential barrier is consistent with the measurements in which very cold neutrons ($\lambda = 24 \text{ \AA}$) are reflected from an oscillating mirror.⁹ This system was modeled as a one-dimensional step potential whose boundary oscillated in time. It was found that the reflected neutron energy spectra were quantized corresponding to the oscillation of the reflecting disk, a result that is comparable to the analytical and numerical results of Ref. 2. In one of the measurements of Ref. 9 the oscillation frequency was 693 kHz and the scattered neutron spectra displayed peaks at $\pm 2.8 \text{ neV}$, consistent with Eq. (9). Additional satellite peaks appeared in their data as the amplitude of the mirror oscillation increased. This result is consistent with our computations, but is not discussed here.

III. SCATTERING FROM A TRAVELING WAVE

A. Static locally periodic potential

The reflectivity and transmission of locally periodic potentials have been studied analytically and numerically.^{23–25} This class of potentials is characterized by a small number of repeating units. One of the reasons for examining the transmission and reflection properties of such potentials, in contrast to a periodic potential which is infinite in extent, is that it can be an efficient means to access numerically the precursors of the properties of periodic potentials, such as band structure.²⁴ Also, the periodic time-variation of these potential may offer additional insight into non-stationary phenomena. The prominent reflection peaks present in periodic potentials can be used as a reference feature to examine the effects of time-dependence.

We consider a localized sinusoidal potential, $V(x - x_V)$, in which $V(\xi)$ has the form:

$$V(\xi) = \begin{cases} V_0 \sin(Q_{lp} \xi) & -w/2 \leq \xi < w/2 \\ 0 & \text{otherwise,} \end{cases} \quad (11)$$

where the one-dimensional reciprocal lattice vector Q_{lp} determines the spatial periodicity via $2\pi/Q_{lp}$, and we choose a width corresponding to an integral number of spatial oscillation periods $w = 11(2\pi/Q_{lp})$. For a barrier with this spatial periodicity, kinematic considerations lead to the Bragg reflection condition in three dimensions: $Q_{lp} = 2k_0 \sin \theta$. In one dimension, this condition corresponds to reflection for $2\theta = \pi$. Thus, we expect a strong reflection when $k_0 = Q_{lp}/2$.

We used our wave packet scattering approach to find the reflectivity shown in Fig. 8. The plane wave reflectivity of $V(x)$ was determined using well-known matrix methods.^{5,7,14} This result was then used with Eq. (5) to determine the theoretical wave packet reflectivity. The agreement of the reflectivity from the wave packet experiments and the theoretical result is excellent over the wave-number range probed. As expected, the first peak in the reflectivity is near $k_0 = 600$.²⁶ The width of the Bragg peak

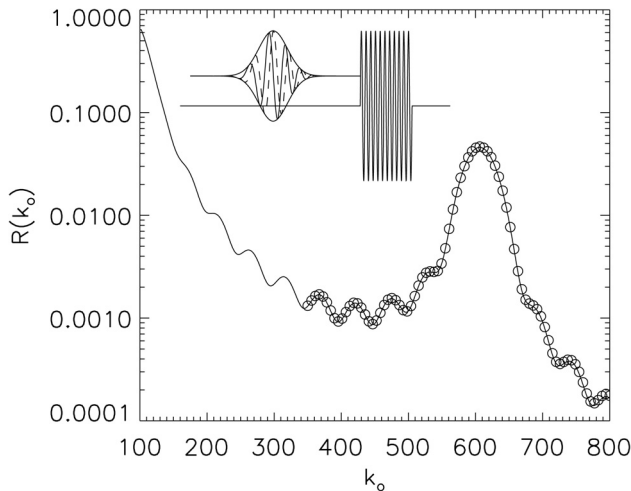


Fig. 8. Reflectivity of the wave packet from a static locally periodic potential; the parameters are $\sigma_x = 0.05$, $V_0 = 5 \times 10^3$, and $Q_{lp} = 1200$. The solid line is the result of a calculation of the plane wave reflectivity integrated over the wave packet via Eq. (5). The circles are the result of the numerical reflectivity simulations described in the text.

near $k_0 = 600$ is broad by design so that the finite width of the wave packet does not smooth out this prominent reflection peak.

B. Traveling wave potential

We now consider the dynamical version of Eq. (11) in which the peaks and troughs of the potential move with a speed v_b , while the extent of the potential remains fixed in space. We choose the sign of v_b so that the traveling wave moves either to the left $v_b < 0$ or to the right $v_b > 0$. The modified expression for the potential centered on x_V is given by $V(x - x_V)$, with

$$V(\xi) = \begin{cases} V_0 \sin(Q_{lp}(\xi - v_b t)) & -w/2 \leq \xi < w/2 \\ 0 & \text{otherwise,} \end{cases} \quad (12)$$

and where v_b is the speed of the traveling wave. The results of the traveling wave moving parallel ($v_{wp} \parallel v_b$) and anti-parallel ($v_{wp} \parallel -v_b$) to the incident wave packet are shown in Fig. 9. The difference between these two cases and the static reflectivity is clear. The reflection peaks for the parallel and anti-parallel cases are equally spaced on either side of the static peak and are Doppler-shifted.

It can be shown that a matter wave that is Bragg reflected in backscattering geometry from a moving periodic lattice has its energy shifted from the static case E_0 by an amount

$$\Delta E = E_0[2(v_b/v_{wp}) + (v_b/v_{wp})^2], \quad (13)$$

where the wave packet's central velocity $v_{wp} = \hbar k_0/m$. Note that Eq. (13) holds for the parallel case, and the sign of v_b must be changed for the anti-parallel case.

Equation (13) is not typically covered in solid state physics courses. However, the concepts and mathematics are sufficiently straightforward so that it can be presented to upper-division undergraduate students. A detailed presentation and derivation are given in Appendix D.

For the parallel case we convert Eq. (13) to an expression in terms of the wavenumber,

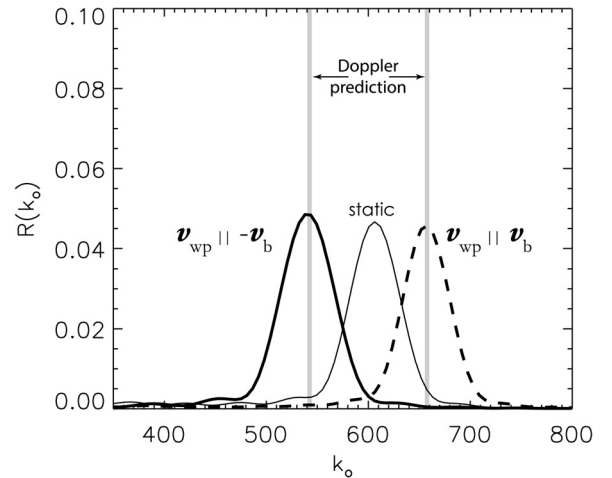


Fig. 9. Reflectivity of the wave packet from a traveling wave in a locally periodic potential; the potential parameters are $Q_{lp} = 1200$, $V_0 = 5 \times 10^3$, $\sigma_x = 0.05$, and $v_b = \pm 57.6$. The static peak is the same as that shown in Fig. 8 except the latter uses a linear rather than a logarithmic scale.

$$k_r = k_0 \sqrt{1 + 2(v_b/v_{wp}) + (v_b/v_{wp})^2}, \quad (14)$$

where k_r is the Doppler-shifted wavenumber. By using the parameters from our solution to the TDSE for the parallel and anti-parallel cases in Eq. (14), we find a Bragg peak shift to $k_r = 658$ in the parallel case and $k_r = 542$ in the anti-parallel case, in excellent agreement with the results shown in Fig. 9.

The Doppler effect for matter waves has been verified in numerous circumstances. It is an essential part of the operation of a neutron backscattering spectrometer in which neutrons are back-reflected from an oscillating crystal monochromator.²⁷ Neutrons of different wavenumbers satisfy the Bragg condition at different times corresponding to the crystal velocity. Thus, it is possible to sweep through a number of different neutron energies by recording the time at which a neutron reflects from the monochromator. A numerical example is provided in Appendix D.

Because a moving potential yields a distinct shift in the Bragg peak based on its direction with respect to the wave packet's direction, we expect that a potential composed of two equal but oppositely moving waves will split the static reflection peak, with some portion of the peak reflected to higher wavenumbers and some to lower wavenumbers.

To test the hypothesis that a superposition of two traveling waves on a potential will split the static Bragg peak reflection, we use the potential $V(x - x_1, t)$ from which we scattered wave packets of different incident wavenumbers, k_0 :

$$V(\xi, t) = \begin{cases} V_0[1 + \cos(\omega t) \sin(Q_{lp}\xi)], & 0 \leq \xi < w \\ 0, & \text{otherwise.} \end{cases} \quad (15)$$

The amplitude of the sinusoid oscillates in time as a standing wave, which is equivalent to two opposing traveling waves.

The following parameters for the potential were used in our computations: $V_0 = 5 \times 10^3$, $\omega = 69167$, $Q_{lp} = 1200$, $w = 11(2\pi/Q_{lp})$, and $x_1 = 0.1$. The wave packet width parameter was $\sigma_x = 0.05$. The resulting reflectivity from this potential as determined using this wave packet scattering technique is shown in Fig. 10. The resulting scattering seen in Fig. 10 illustrates the expected splitting. In the static case, the Bragg peak appears at a wavenumber $k_0 = 606$. The Doppler equation predicts that the shifted peaks occur at $k = k_0 \pm 58$, and as can be seen from Fig. 10 the agreement with the prediction is excellent.

The phenomenon of Doppler-shifted peaks arising from reflection from potential oscillations has been observed experimentally. Hamilton and Klein measured the neutrons reflected from a surface acoustic wave on a quartz crystal.²⁸ The surface acoustic waves were generated on the quartz by placing periodically-spaced transducers on the surface (through photolithography) and driving them at a frequency of 34.5 MHz, resulting in a traveling wave with wavelength $\lambda = 91.5 \mu\text{m}$ and amplitude of 13.5 Å. Although the surface acoustic waves were traveling waves in the plane of the substrate, they locally present a standing wave perpendicular to the surface, accessible via the component of the reflected beam perpendicular to the surface. Thus, their experimental situation is comparable to the one we consider. Their measurements showed that the component of the reflected neutrons perpendicular to the surface results in a diffraction

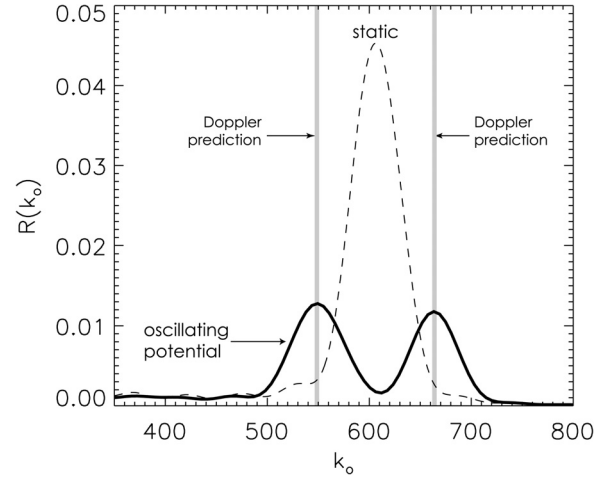


Fig. 10. Comparison of the reflectivity from a static locally-periodic potential (dashed curve) to that of a locally-periodic potential in which the amplitude oscillates periodically in time (solid curve). There is a single Bragg peak evident in the static case, which is expected based on the spatial periodicity of the potential. For the case in which the amplitude oscillates in time, the Bragg peak splits into two parts equally spaced on either side of the peak corresponding to the static case. The gray vertical lines through the split peaks denote the expected peak locations based on the Doppler shift. The parameters of the calculation are given in the text.

pattern. When there was no surface acoustic wave present, there was no diffraction pattern. When a surface acoustic wave is present, the standing wave creates the time-dependent “diffraction” grating and results in two diffraction peaks. Our numerical computations of wave packets reflecting from a traveling wave potential are consistent with these neutron experiments.

IV. CONCLUSIONS

Although numerical solutions of the TDSE have been used for many years to explore the reflection and transmission properties of potential barriers of varying complexity, there has not been as extensive an application of these techniques to time-varying barriers. The use of absorbing boundary conditions coupled with “measurements” of probability current at two distinct locations permit relatively small integration domains for solving the TDSE, thus making estimates of reflectivity and transmission probabilities easily accessible with modest computational resources. We discussed applications of the technique to several time-varying potentials in which the reflection probability was probed by examining the differences of the reflection probability from the static barrier case. In each of the systems, the reflection probability was correlated with inelastic processes in which the wave packets gain and/or lose energy from interacting with the barrier. The phenomena observed in these computations are comparable to non-stationary phenomena observed in many types of neutron scattering experiments with vibrating mirrors and moving diffraction gratings, as described, for example, in Ref. 10.

V. SUGGESTED PROBLEMS

1. Show that if we write the wavefunction satisfying the TDSE explicitly as $\psi(x, t) = R(x, t) + iI(x, t)$ where $R(x, t)$

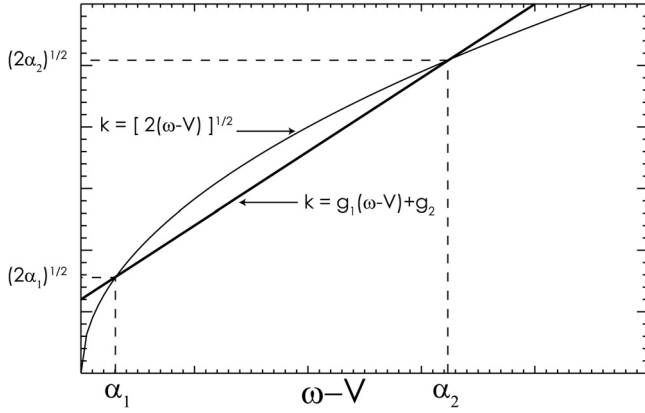


Fig. 11. Schematic representation showing Shibata's linear approximation to the nonlinear dispersion relation for the Schrödinger equation.

- and $I(x, t)$ are real-valued functions, the following two coupled partial differential equations must be satisfied: $\dot{R}(x, t) = -\hbar I''/2m + VI/\hbar$ and $\dot{I}(x, t) = \hbar R''/2m - VR/\hbar$, where $f' \equiv \partial f/\partial x$.
- Use the result from Problem 1, but for the dimensionless TDSE ($\hbar = m = 1$), and the central difference approximation for a derivative of a function to derive Eqs. (B1) and (B2). Hint: You will need to assume that R is updated in time before I to match Eqs. (B1) and (B2). Recall that the central difference approximation for a derivative of a function is given by $\partial f/\partial x \simeq [f(x + \delta x/2) - f(x - \delta x/2)]/\delta x$.
 - Show that the dispersion relation at the right-most boundary for an incident plane wave $\psi(x, t) = e^{i(kx - \omega t)}$ yields no reflected component if $k = \sqrt{2(\omega - V)}$, where V is evaluated at the boundary. Hint: In general, the valid dispersion relations for the TDSE are $k = \pm \sqrt{2(\omega - V)}$, but we purposefully neglected solutions with negative wave-numbers. Why?
 - (a) Use the construction in Fig. 11 to derive the expressions for g_1 and g_2 in Eqs. (B4) and (B5) as functions of α_1 and α_2 . (b) Use the plane-wave solution to the free-particle ($V = 0$) TDSE $\psi(x, t) = e^{i(kx - \omega t)}$ to show that Eq. (B6) corresponds to Eq. (B3).
 - Show that if $\psi(x, t) = R(x, t) + iI(x, t)$ satisfies Eq. (B6), then Eqs. (B7) and (B8) must be satisfied.
 - Show that if $\psi(x, t) = R(x, t) + iI(x, t)$, then the probability current can be written as $j(x, t) = \hbar(RI' - IR')/m$.

ACKNOWLEDGMENTS

The author wishes to acknowledge many useful and enlightening discussions with Chuck Majkrzak as well as his encouragement to publish this work. He also wishes to thank Bill Hamilton, Brian Maranville, Brian Kirby, Mike Rowe, and Peter Gehring for helpful discussions.

APPENDIX A: SCALING THE SCHRÖDINGER EQUATION

It is straightforward to move between the dimensionless TDSE

$$i\frac{\partial\psi}{\partial t} = -\frac{1}{2}\frac{\partial^2\psi}{\partial x^2} + V(x, t)\psi(x, t), \quad (\text{A1})$$

with dimensionless position and time increments Δx and Δt , and its form with dimensions $\Delta\tilde{x}$ and $\Delta\tilde{t}$

$$i\hbar\frac{\partial\psi}{\partial\tilde{t}} = -\frac{\hbar^2}{2m}\frac{\partial^2\psi}{\partial\tilde{x}^2} + \tilde{V}(\tilde{x}, \tilde{t})\psi(\tilde{x}, \tilde{t}). \quad (\text{A2})$$

The connection is established using the relations $\Delta\tilde{x} = (\hbar/\sqrt{m\alpha})\Delta x$ and $\Delta\tilde{t} = (\hbar/\alpha)\Delta t$. Selecting the free parameter α permits us to specify the scale of one of the variables. For example, if we use the mass of the neutron $m_n = 939.6$ MeV/c², specify the spatial increment as $\Delta x = 1$ and $\Delta\tilde{x} = 1500$ Å, then the time increment corresponding to $\Delta t = 1$ is $\Delta\tilde{t} = 0.36$ μs. This choice implies that for $k = 400$, $\tilde{k} = 0.27$ Å⁻¹ or $\tilde{\lambda} = 2\pi/\tilde{k} = 23.5$ Å. In addition, the potential scales as $\tilde{V} = \alpha V$, so that a barrier height $V_0 = 4 \times 10^5$ corresponds to a height of $\tilde{V}_0 = 0.74$ meV.

APPENDIX B: NUMERICAL SOLUTION OF THE SCHRÖDINGER EQUATION WITH ABSORBING BOUNDARY CONDITIONS

The solution of the dimensionless Schrödinger equation is performed using the finite-difference time-domain approach of Visscher,¹⁷ augmented by boundary conditions as discussed by Shibata.²⁰ Space is discretized over M points via $x_m = m\Delta x$, where $m = 0, 1, \dots, (M - 1)$. Time is discretized, but the real and imaginary components of the wavefunction are evaluated at time steps that differ by $\Delta t/2$. The real and imaginary components $R_{m,n}$ and $I_{m,n}$ (where $\psi_{m,n} = R_{m,n} + iI_{m,n}$) are approximations such that $R_{m,n} = R(m\Delta x, n\Delta t)$ and $I_{m,n} = I(m\Delta x, (n + 1/2)\Delta t)$. The wavefunction is updated at all points in the spatial mesh except at the boundaries using the two-step sequence:

$$R_{m,n+1} = R_{m,n} + \frac{1}{2}\frac{\Delta t}{(\Delta x)^2} [2I_{m,n} - I_{m+1,n} - I_{m-1,n}] + \Delta t V_{m,n} I_{m,n}, \quad (\text{B1})$$

$$I_{m,n+1} = I_{m,n} - \frac{1}{2}\frac{\Delta t}{(\Delta x)^2} [2R_{m,n+1} - R_{m+1,n+1} - R_{m-1,n+1}] - \Delta t V_{m,n+1} R_{m,n+1}. \quad (\text{B2})$$

The values of the real and imaginary components at the boundaries, $R_{0,n}$, $R_{(M-1),n}$, $I_{0,n}$, and $I_{(M-1),n}$, are obtained by imposing the absorbing boundary conditions. The absorbing boundary conditions take the form of a set of partial differential equations imposed at the boundaries that represent a specific dispersion relation designed to annihilate incoming plane waves. For a plane wave moving toward the right boundary $\psi(x, t) = e^{i(kx - \omega t)}$, the following dispersion relation imposed at that boundary ensures that the wave will be annihilated: $k = \sqrt{2(\omega - V)}$ (see Problem 3). For a left moving wave, the following dispersion relation annihilates the incoming wave: $k = -\sqrt{2(\omega - V)}$. Neither of these dispersion relations can be converted into a differential equation so Shibata made the following linear approximation:

$$k = g_1(\omega - V) + g_2, \quad (\text{B3})$$

with

$$g_1 = \pm \frac{\sqrt{2\alpha_2} - \sqrt{2\alpha_1}}{\alpha_2 - \alpha_1} \quad (\text{B4})$$

$$g_2 = \pm \frac{\alpha_2 \sqrt{2\alpha_1} - \alpha_1 \sqrt{2\alpha_2}}{\alpha_2 - \alpha_1}. \quad (\text{B5})$$

The \pm corresponds to right- and left-moving waves, respectively. This approximation is illustrated in Fig. 11.

To specify g_1 and g_2 in Eqs. (B4) and (B5) we need to select α_1 and α_2 . This choice is straightforward because we can make the selection based on the energy of the initial wavefunction. For Gaussian wave packets with a central wavenumber, k_0 , we chose α_1 and α_2 so that they bracket the energy: $\alpha_1 < k_0^2/2 < \alpha_2$. This choice was made automatically by extracting the width of the peak of the momentum distribution for the initial Gaussian wave packet (full-width at half maximum) and selecting values of α_1 and α_2 corresponding to the width of the momentum distribution.

Converting Eq. (B3) into a partial differential equation yields (see Problem 4)

$$i\dot{\psi} = \left[-i \frac{1}{g_1} \frac{\partial}{\partial x} + V - \frac{g_2}{g_1} \right] \psi. \quad (\text{B6})$$

The corresponding coupled partial differential equations for the real and imaginary parts of the wavefunction are

$$\dot{R} = -\frac{1}{g_1} \frac{\partial R}{\partial x} + \left(V - \frac{g_2}{g_1} \right) I \quad (\text{B7})$$

$$\dot{I} = -\frac{1}{g_1} \frac{\partial I}{\partial x} - \left(V - \frac{g_2}{g_1} \right) R. \quad (\text{B8})$$

Equations (B7) and (B8) can be converted to a set of coupled finite-difference time-domain equations. At the left boundary ($m=0$), the result is

$$R_{0,n+1} = R_{0,n} + R_{1,n} - R_{1,n+1} - \frac{2}{g_1} \frac{\Delta t}{\Delta x} (R_{1,n} - R_{0,n}) + \left(V_{0,n} - \frac{g_2}{g_1} \right) (I_{0,n} + I_{1,n}) \Delta t, \quad (\text{B9})$$

$$I_{0,n+1} = I_{0,n} + I_{1,n} - I_{1,n+1} + \frac{2}{g_1} \frac{\Delta t}{\Delta x} (I_{1,n} - I_{0,n}) - \left(V_{0,n+1} - \frac{g_2}{g_1} \right) (R_{0,n} + R_{1,n}) \Delta t. \quad (\text{B10})$$

At the right boundary ($m=M-1$), the result is

$$R_{M-1,n+1} = R_{M-1,n} + R_{M-2,n} - R_{M-2,n+1} - \frac{2}{g_1} \frac{\Delta t}{\Delta x} (R_{M-1,n} - R_{M-2,n}) + \left(V_{M-1,n} - \frac{g_2}{g_1} \right) (I_{M-1,n} + I_{M-2,n}) \Delta t, \quad (\text{B11})$$

$$I_{M-1,n+1} = I_{M-1,n} + I_{M-2,n} - I_{M-2,n+1} + \frac{2}{g_1} \frac{\Delta t}{\Delta x} (I_{M-1,n} - I_{M-2,n}) - \left(V_{M-1,n+1} - \frac{g_2}{g_1} \right) (R_{M-1,n} + R_{M-2,n}) \Delta t. \quad (\text{B12})$$

Equations (B9)–(B12) are updated immediately after the updates are made using Eqs. (B1) and (B2). To ensure that the solutions are stable,¹⁷ we set $\Delta t/(2(\Delta x)^2)$ equal to a constant less than 1. In all cases, our solutions were stable for a constant of 0.075.

APPENDIX C: PROBABILITY CURRENT AND TRANSMISSION PROBABILITY

It is straightforward to show that the transmission probability of a wave packet that has crossed a spatially bounded region with a potential can be found by integrating the probability current at a point beyond that region for all times, as stated in Eq. (6). We use the scattering geometry shown in Fig. 1 but assume that the computational boundaries expand from $0 \leq x \leq L$ to $-\infty < x < \infty$.

Conservation of probability in one dimension is given by

$$\frac{\partial P}{\partial t} + \frac{\partial j}{\partial x} = 0, \quad (\text{C1})$$

where $P(x, t) = |\psi(x, t)|^2$ and $j(x, t)$ is given by Eq. (7).¹³ Our “detector” for transmitted current is at $x = x_t$. We assume that the wave packet moves from the region $x < x_t$ so that $j(x > x_t, t) = 0$ for $t \leq 0$. For $t \geq 0$, the wave packet crosses the boundary $x = x_t$.

We next integrate Eq. (C1) over the region $x \in [x_t, \infty)$ and from the time that the wave packet starts to move across the boundary $x = x_t$ at $t = 0$:

$$0 = \int_0^t dt' \int_{x_t}^{\infty} dx \frac{\partial P}{\partial t'} + \int_0^t dt' \int_{x_t}^{\infty} dx \frac{\partial j}{\partial x} = \int_{x_t}^{\infty} dx P(x, t') \Big|_{t'=0}^t + \int_0^t dt' j(x, t') \Big|_{x=x_t}^{\infty}. \quad (\text{C2})$$

We have

$$\int_{x_t}^{\infty} dx P(x, 0) = 0, \quad (\text{C3})$$

because the wave packet is not in the region $x \in [x_t, \infty)$ prior to $t=0$. Also, because $\psi(x, t) \rightarrow 0$ as $x \rightarrow \pm\infty$, we have $j(x, t) \rightarrow 0$ as $x \rightarrow \pm\infty$, which gives

$$\int_0^t dt' j(x_t, t') = \int_{x_t}^{\infty} dx P(x, t). \quad (\text{C4})$$

If we let the upper bound on the time integral go to infinity, the spatial integral of $P(x, t)$ over the region $x > x_t$ is the transmission probability T . Therefore, we have

$$\int_0^{\infty} dt' j(x_t, t') = T, \quad (\text{C5})$$

which is the desired result. A similar argument can be used to show that

$$\int_0^{\infty} dt' j(x_r, t') = -R. \quad (\text{C6})$$

APPENDIX D: DERIVATION OF THE DOPPLER SHIFT FOR MATTER WAVES IN BACKSCATTERING GEOMETRY

The Bragg condition for a matter wave incident on a stationary lattice with lattice spacing d is

$$\lambda_0 = 2d \sin \theta, \quad (\text{D1})$$

where λ_0 is the wavelength of the incident matter wave and 2θ is the scattering angle. Because $Q = 2\pi/d$ and $k_0 = 2\pi/\lambda_0$, the Bragg condition can be written as

$$Q = 2k_0 \sin \theta. \quad (\text{D2})$$

In backscattering geometry, $2\theta = \pi$ so that $\lambda_0 = 2d$ and $Q = 2k_0$. The speed of the incident matter wave is given by

$$v_0 = \frac{h}{m\lambda_0} = \frac{h}{2md}, \quad (\text{D3})$$

and its energy is

$$E_0 = \frac{h^2}{8md^2}. \quad (\text{D4})$$

The shift in energy of the matter wave reflected from the moving lattice is found via $\Delta E = E_V - E_0$, where E_0 is the energy of the reflected matter wave when the crystal is at rest [see Eq. (D4)], and E_V is the energy of the matter wave that has been reflected from the moving lattice. To determine E_V , we use the reciprocal lattice construction due to Buras and Giebultowicz,²⁹ shown in Fig. 12, where the triangle ABC illustrates the scattering geometry from the moving lattice in the laboratory (stationary) frame and the triangle ABD shows the scattering geometry in the moving frame. The incident and reflected matter wave velocities are denoted \mathbf{v}_0 and \mathbf{v}_r , respectively; the corresponding velocities in the moving frame are \mathbf{u}_0 and \mathbf{u}_r . From Fig. 12, we see that the initial and final velocities in the laboratory frame satisfy the condition

$$\mathbf{v}_r = \mathbf{v}_0 + \frac{\hbar \mathbf{Q}}{m}. \quad (\text{D5})$$

If the lattice were stationary, then the triangle ABC would be an isosceles triangle with $\mathbf{v}_0 = \mathbf{v}_r$ and $\theta_i = \theta_r$, and would be equivalent to triangle ABD. However, Fig. 12 illustrates that the effect of the lattice moving with velocity \mathbf{V} is a translation and distortion of the scattering triangle ABC in the laboratory frame. The scattering triangle ABD in the moving frame is an isosceles triangle with $\mathbf{u}_0 = \mathbf{u}_r$. We can calculate the length of the vector \overline{AB} (or $\hbar\mathbf{Q}/m$). Because $v_0 = \hbar/2md$ it is easy to show that $\hbar\mathbf{Q}/m = 2v_0$. Because the dashed line perpendicular to \overline{AB} that terminates at D bisects \overline{AB} , half of the length of \overline{AB} is v_0 .

With this information and the geometry in Fig. 12, we can calculate $2d \sin \theta_r$ to be

$$\begin{aligned} 2d \sin \theta_r &= 2d \left(\frac{v_0 + V}{v_r} \right) = \frac{\lambda_0 v_0}{v_r} (1 + V/v_0) \\ &= \lambda_r (1 + V/v_0), \end{aligned} \quad (\text{D6})$$

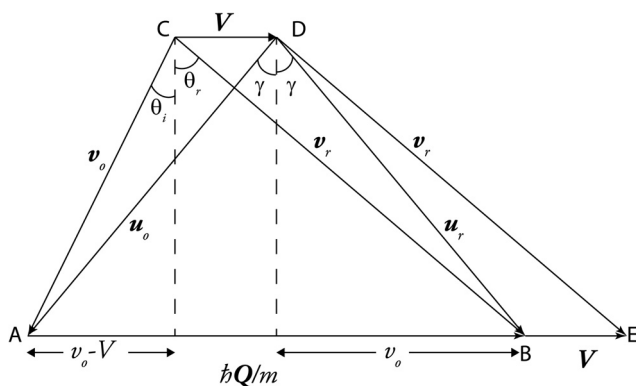


Fig. 12. The modified Ewald construction for reflection from a moving lattice.²⁹

where we used the relation $v_0\lambda_0 = h/m = v_r\lambda_r$ in the last step. Rewriting Eq. (D6) (using $2\theta_r = \pi$) yields

$$\lambda_r = \frac{2d}{1 + V/v_0}. \quad (\text{D7})$$

The energy of the reflected matter wave can be determined using the expressions:

$$E_V = \frac{p_r^2}{2m} = \frac{h^2}{2m\lambda_r^2} = \frac{h^2}{8md^2} \left[1 + \frac{V}{v_0} \right]^2 = E_0 \left[1 + \frac{V}{v_0} \right]^2. \quad (\text{D8})$$

Finally, we can compute the energy shift

$$\begin{aligned}\Delta E &= E_V - E_0 = E_0 \left[1 + \frac{V}{v_0} \right]^2 - E_0 \\ &= E_0 \left[2 \left(\frac{V}{v_0} \right) + \left(\frac{V}{v_0} \right)^2 \right].\end{aligned}\tag{D9}$$

The substitution $V = v_b$ and $v_0 = v_{\text{wp}}$ yields Eq. (13).

A straightforward application of the Doppler energy shift equation is the Doppler monochromator system for the NIST High Flux Backscattering Spectrometer.²⁷ The monochromator is tiled with Si wafers and oscillates sinusoidally in time with an amplitude $A = 4.5$ cm at an adjustable frequency. Neutrons undergo Bragg scattering in the backscattering geometry from the (111) reflection of Si. The lattice spacing for this reflection is $d = 3.135$ Å. Thus neutrons of wavelength $\lambda_0 = 2d = 6.271$ Å are reflected when the monochromator is stationary. The speed of a neutron with this wavelength is $v_0 = 631.39$ m/s and the energy is $E_0 = 2080.11$ μeV. The energy of the neutrons reflected from the oscillating monochromator is time-dependent. If we substitute one of the operating frequencies of the NIST Doppler system ($f = 18$ Hz), the result is

$$\Delta E(t) = E_0 \left[\frac{2\omega A \cos \omega t}{v_0} + \left(\frac{\omega A \cos \omega t}{v_0} \right)^2 \right] \quad (\text{D10a})$$

$$= 33.5 \cos(113.1t) + 0.14 \cos^2(113.1t). \quad (\text{D10b})$$

Thus, the dynamic range of the spectrometer at this operating frequency is about $\pm 33.6 \mu\text{eV}$.

^{a)}Electronic mail: robert.dimeo@nist.gov

¹A. Goldberg, H. M. Schey, and J. L. Schwartz, "Computer-generated motion pictures of one-dimensional quantum-mechanical transmission and reflection phenomena," *Am. J. Phys.* **35**(3), 177–186 (1967).

²D. L. Haavig and R. Reifenberger, “Dynamic transmission and reflection phenomena for a time-dependent rectangular potential,” *Phys. Rev. B* **26**(12), 6408–6420 (1982).

³M. L. Chiofalo, M. Artoni, and G. C. La Rocca, “Atom resonant tunnelling through a moving barrier,” *New J. Phys.* **5**, 78.1–78.15 (2003).

⁴M. R. A. Shegelski, T. Poole, and C. Thompson, “Capture of a quantum particle by a moving trapping potential,” *Eur. J. Phys.* **34**, 569–590 (2013).

³J. Penfold and R. K. Thomas, "The application of the specular reflection of neutrons to the study of surfaces and interfaces," *J. Phys.: Condens. Matter* **2**, 1369–1412 (1990).

2. J. F. Ankner, C. F. Majkrzak, and S. K. Satija, "Neutron reflectivity and grazing angle diffraction," *J. Res. Natl. Inst. Stand. Technol.* **98**(1), 47-58 (1993).

⁷J. Lekner, "Reflection of neutrons by periodic stratifications," *Physica B* **202**, 16–22 (1994).

- ⁸E. Raitman, V. Gavrilov, and Ju. Ekmanis, "Neutron diffraction on acoustic waves in perfect and deformed single crystals," in *Modeling and Measurement Methods for Acoustic Waves and for Acoustic Microdevices*, edited by Marco G. Beghi (InTech, 2010).
- ⁹J. Felber, R. Gähler, and C. Rausch, "Matter waves at a vibrating surface: Transition from quantum-mechanical to classical behavior," *Phys. Rev. A* **53**(1), 319–328 (1996).
- ¹⁰M. Utsuro and V. K. Ignatovich, *Handbook of Neutron Optics* (Wiley-VCH, Verlag GmbH & Co. KGaA, 2010).
- ¹¹A. Steane, P. Szriftgiser, P. Desbiolles, and J. Dalibard, "Phase modulation of atomic de Broglie waves," *Phys. Rev. Lett.* **74**(25), 4974–4975 (1995).
- ¹²A. Messiah, *Quantum Mechanics* (Dover Publications, New York, 1999).
- ¹³R. W. Robinett, *Quantum Mechanics: Classical Results, Modern Systems, and Visualized Examples* (Oxford U.P., New York & Oxford, 1997).
- ¹⁴R. Gilmore, *Elementary Quantum Mechanics in One Dimension* (The Johns Hopkins University Press, Baltimore & London, 2004).
- ¹⁵M. H. Bramhall and B. M. Casper, "Reflections on a wave packet approach to quantum mechanical barrier penetration," *Am. J. Phys.* **38**(9), 1136–1145 (1970).
- ¹⁶A specific exception is for the case in which a barrier moves with constant velocity, v_b . If the reflectivity $R(k_0)$ of the static barrier is known, then the reflectivity of the moving barrier is simply a shifted version of the static reflectivity, $R(k_0 - mv_b/\hbar)$.
- ¹⁷P. B. Visscher, "A fast explicit algorithm for the time-dependent Schrödinger equation," *Comput. Phys.* **5**(6), 596–598 (1991).
- ¹⁸W. Dai, G. Li, R. Nassar, and S. Su, "On the stability of the FDTD method for solving a time-dependent Schrödinger equation," *Numer. Methods Partial Differ. Equ.* **21**(6), 1140–1154 (2005).
- ¹⁹We tested the accuracy of the algorithm by integrating the wave packet forward in time for N time steps, during which it interacted with a time-varying potential. After N time steps the wave function was replaced by its complex conjugate and then integrated for another N time steps forward in time (but the potential motion was reversed). The resulting wave packet moved backward in time as expected, eventually lying on top of the initial wave packet. The difference between the initial and final wave packet probability densities integrated over the full-width at half maximum was 0.005%.
- ²⁰T. Shibata, "Absorbing boundary conditions for the finite-difference time-domain calculation of the one-dimensional Schrödinger equation," *Phys. Rev. B* **43**(8), 6760–6763 (1991).
- ²¹T. Paul, M. Hartung, K. Richter, and P. Schlagheck, "Nonlinear transport of Bose-Einstein condensates through mesoscopic waveguides," *Phys. Rev. A* **76**, 063605-1–22 (2007).
- ²²F. L. Dubeibe, "Solving the time-dependent Schrödinger equation with absorbing boundary conditions and source terms in Mathematica 6.0," *Int. J. Mod. Phys. C* **21**(11), 1391 (2010).
- ²³H.-W. Lee, A. Zysnarski, and P. Kerr, "One-dimensional scattering by a locally periodic potential," *Am. J. Phys.* **57**(8), 729–734 (1989).
- ²⁴D. J. Griffiths and N. F. Taussig, "Scattering from a locally periodic potential," *Am. J. Phys.* **60**(10), 883–888 (1992).
- ²⁵D. J. Griffiths and C. A. Steinke, "Waves in locally periodic media," *Am. J. Phys.* **69**(2), 137–154 (2001).
- ²⁶Upon closer inspection, the peak location is actually closer to $k_0 = 606$. This shift in the peak is due to dynamical effects as described in Ref. 7, Sec. 4.
- ²⁷A. Meyer, R. M. Dimeo, P. M. Gehring, and D. A. Neumann, "The high-flux backscattering spectrometer at the NIST Center for Neutron Research," *Rev. Sci. Instrum.* **74**(5), 2759–2777 (2003).
- ²⁸W. A. Hamilton, A. G. Klein, G. I. Opat, and P. A. Timmins, "Neutron diffraction by surface acoustic waves," *Phys. Rev. Lett.* **58**(26), 2770–2773 (1987).
- ²⁹B. Buras and T. Giebultowicz, "Modified Ewald construction for neutrons reflected by moving lattices," *Acta Crystallogr.* **28**(2), 151–153 (1972).



Milvay Earth Inductor

"Milvay" was the house brand of the Chicago Apparatus Company. The Earth Inductor was used in an experiment to measure the horizontal and vertical components of the earth's magnetic field. With the apparatus oriented as in the photograph with the axis of the coil pointing east-west, the coil was flipped, and the resulting signal was integrated with a ballistic galvanometer to give the vertical component; standing the apparatus upright and flipping the coil gave the horizontal component. This was a standard electrical measurements experiment until the nineteen sixties; it might well be revived with operational amplifiers used for the integration. The competition used wood construction; this one is all aluminum, apart from the fastenings. It cost \$60 in 1929, and is in the Greenslade Collection. (Notes and photograph by Thomas B. Greenslade, Jr., Kenyon College)